Journal of Alloys and Compounds 1044 (2025) 184280

Contents lists available at ScienceDirect

Journal of Alloys and Compounds

journal homepage: www.elsevier.com/locate/jalcom

Research article

Mass transport and structural transformations in core@shell Cu@Ni nanoparticles

Luca Benzi [a], Diana Nelli [a,*], Christine Mottet [b], Riccardo Ferrando [a,*]

[a] Physics Department, University of Genoa, Via Dodecaneso 33, Genoa, 16146, Italy
[b] Aix-Marseille University/CNRS, CINaM UMR 7325, Campus de Luminy, Marseille, 13288, France

ARTICLE INFO

Keywords:
Core-shell nanoparticles
Diffusion
Copper
Nickel
Molecular dynamics

ABSTRACT

Core@shell Cu@Ni nanoalloys are of interest for applications to catalysis, magnetism and flexible electronics. The Cu@Ni chemical arrangement is however strongly out of equilibrium, because the two metals show some preferential tendency to mix instead of forming phase-separated structures, and Cu atoms tend to segregate to the surface because of the lower cohesion and surface energy of Cu with respect to Ni. Here we study the evolution towards equilibrium of Cu@Ni nanoparticles by molecular dynamics simulations. We consider different sizes from about 150 to about 1000 atoms. The simulations allow to single out the mechanisms by which Cu atoms leave the core and then pass through the Ni shell to reach the nanoparticle surface. Some of these mechanisms involve a single Cu atom moving to the surface, while other mechanisms bring many Cu atoms to the surface at the same time. The latter mechanisms are associated to deep structural transformations of the entire nanoparticle. The simulations show also that the detachment of a Cu atom from the core involves the formation of a vacancy, which may migrate within the nanoparticle. We calculate the energy barriers for vacancy diffusion in pure Ni and Cu nanoparticles and in Cu@Ni nanoalloys, obtaining a good agreement with the available experimental data.

1. Introduction

Core@shell arrangements [1] offer the possibility of protecting unstable cores to preserve their properties. In metallic nanoalloys [2], there are many examples of core@shell structures for applications in magnetism, plasmonics and catalysis [3–5]. When the core@shell arrangement is the equilibrium configuration of the nanoalloy, the protection of the core can be effective and stable against ageing. However, in many cases, core@shell structures are produced in out-of-equilibrium conditions [6]. In these cases, it is interesting to study their possible evolution towards equilibrium [7,8]. For some applications, it may be important to slow down the evolution to preserve the non-equilibrium core@shell configurations for as long as possible, while in other cases it may be interesting to activate and control the evolution towards equilibrium.

From this point of view, Cu@Ni nanostructures are a very interesting case. The NiCu bulk alloy is miscible for all compositions for temperatures above 600 K, presenting a miscibility gap below that temperature [9,10]. Copper has lower surface energy and cohesive energy than nickel [11,12], therefore some surface segregation of Cu is expected in nanostructures, as shown in experiments and simulations [10,13,14]. In general, the equilibrium configuration of a NiCu nanoparticle is expected to have a Cu-enriched surface and some competition between mixing and phase separation in the interior. The actual equilibrium structure depends on the temperature, size and geometric structure of the nanoparticle [10,14–18]. Therefore neither the Cu@Ni nor the Ni@Cu arrangement with a sharp core–shell separation should correspond exactly to the true equilibrium configurations, with the Cu@Ni arrangement being much further from equilibrium than the Ni@Cu one. Therefore, Cu@Ni nanostructures should show a much more pronounced evolution when subjected to ageing, unless they are exposed to certain external environments, such as those rich in oxygen or hydrogen, which favour the surface segregation of nickel [19–22].

Both Ni@Cu and Cu@Ni nanoparticles [23–26] have been produced for applications in the field of magnetism and as catalysts for various chemical reactions [15,16,27–29]. Cu@Ni nanoparticles have been used as glucose sensors [30]. Furthermore, in recent years, Cu@Ni nanowire networks have attracted particular interest for the preparation of flexible and stretchable transparent electrodes [31–37,37–39]. In these electrodes, Cu nanowires are encapsulated in Ni shells to prevent oxidation, as pure Cu nanowires are chemically and thermally unstable. The Ni shell protects the Cu nanowires by forming a very thin layer of nickel oxide on the surface of the shell. However, to allow the

* Corresponding authors.
E-mail addresses: diana.nelli@edu.unige.it (D. Nelli), riccardo.ferrando@unige.it (R. Ferrando).

https://doi.org/10.1016/j.jallcom.2025.184280
Received 15 August 2025; Received in revised form 3 October 2025; Accepted 7 October 2025
Available online 11 October 2025

contact between the copper cores at the junctions between different wires, some form of annealing is necessary, so that the Cu atoms can diffuse through the Ni shell and insure a better electrical contact [40]. Heating can be achieved by a reduction step, in which the thin oxide layer is removed. Therefore, for this type of system, it would be very interesting to understand how Cu atoms can diffuse through a Ni shell in a nanostructure. To this end, molecular dynamics (MD) simulations are a very valuable tool, because they allow diffusion mechanisms to be analysed with atomic resolution.

The diffusion of atoms in clusters and nanoparticles has been the subject of several MD studies. However, most of these studies have considered the diffusion of adatoms or small atomic islands on the surface of nanoparticles [41–47], while studies of diffusion processes within nanoparticles are much less extensive [48].

In this paper, we have studied the elementary diffusion mechanisms that occur in Cu@Ni nanoparticles using MD simulations. Such phenomena, though relevant for experiments and applications, are still largely unknown. In fact, despite the large amount of computational works on CuNi nanoparticles in the literature, studies of the evolution from the out-of-equilibrium core@shell Cu@Ni configuration are lacking. Our simulations, in the form of heating ramps and constant temperature evolutions, have identified the most important diffusion mechanisms, and, in some cases, even complex structural transformations. We have found that the diffusion of Cu atoms from the core of the nanoparticles is related to the formation of atomic vacancies, whose diffusion barriers have been calculated and compared to available experimental data, obtaining a good agreement.

2. Model and methods

An atomistic force field has been used to describe the interactions between atoms. This force field is derived within the second-moment approximation of the tight binding (SMA-TB) model [49], developed by Gupta [50] and by Rosato et al. [51]. The SMA-TB potential is a common choice for modelling nanoparticles made of transition or noble metals. It has been employed in multiple computational works, when, as in this case, the sizes and time scales under investigation were not accessible to ab initio methods. The accuracy of this model has been verified in many studies, by comparing its results and prediction with DFT calculations on small systems and with experimental data. For the metals considered in this work, results of tests against DFT calculations can be found in Refs. [14,52].

In the SMA-TB force field, the potential energy of a system of N atoms is calculated as a sum atomic energies E_i, $i = 1, \ldots, N$. E_i is composed of two contributions: binding E_i^b and repulsive E_i^r

$$E = \sum_i E_i = \sum_i (E_i^b + E_i^r). \tag{1}$$

The binding contribution has the form

$$E_i^b = -\sqrt{\sum_{j \neq i} \xi_{\alpha\beta}^2 \, e^{-2q_{\alpha\beta}\left(\frac{r_{ij}}{r_{\alpha\beta}^0} - 1\right)}}, \tag{2}$$

whereas the repulsive one is

$$E_i^r = \sum_{j \neq i} A_{\alpha\beta} \, e^{-p_{\alpha\beta}\left(\frac{r_{ij}}{r_{\alpha\beta}^0} - 1\right)}. \tag{3}$$

r_{ij} is the distance between the atom i and the atom j; α and β indexes specify the atomic species of atoms i and j; $r_{\alpha\beta}^0$ is the first-neighbour distance in the bulk lattice.

The above form of the potential is valid up to $r_{ij} \leq r_{c1}$; then the potential is brought to zero at distance r_{c2} by a fifth-degree polynomial connection.

In this work, we have used two different SMA-TB force field parameter sets: the former has been fitted on DFT calculation by Panizon et al. [14], while the latter has been fitted on experimental data by Roussel et al. [53]. In the following, they are referred to as DFT-fitted and EXP-fitted parameter sets, respectively. Parameters of the two sets are reported in Table 1.

Monte Carlo (MC) simulations based on the Metropolis algorithm have been carried out in the isothermal–isobaric ensemble (constant number of atoms of each species, temperature and pressure). Two types of MC moves have been applied: random atomic displacements and random chemical exchange between atoms of different species. Two atoms of different species at different random sites are exchanged with probability

$$\min\left[1, \exp\left(-\frac{\Delta E}{k_B T}\right)\right], \tag{4}$$

where ΔE is the energy difference between configurations after and before the exchange move. In a typical simulation, we have performed 3000 macrosteps. In each macrostep, N elementary steps have been made. In an elementary step, an atom is chosen randomly, and it is either randomly displaced for 10 times, or its chemical identity is swapped. We have performed temperature ramps, increasing or decreasing the temperature by steps of 20 degrees.

Molecular dynamics (MD) simulations have been performed using our own code, in which the equations of motion are solved by the velocity Verlet algorithm [54] with a time step of 5 fs. Such time step is small enough to ensure satisfactory energy conservation in microcanonical simulations, as we have checked for our CuNi nanoparticles. After 1 μs at 1100 K (the highest temperature employed in this study), we have measured an energy drift smaller than 0.01% of the initial energy. At lower temperatures, the energy drift is even smaller. As a further validation, we have calculated the melting temperature of a pure Ni truncated octahedron of 586 atoms by two sets of five heating MD simulations, with heating rate $r_h = 1$ K/ns; in the first set, we have used a timestep of 5 fs, whereas in the second set, we have used 2 fs. The results obtained in the two cases, averaged over the five simulations performed, are fully compatible ($T_m = (1128 \pm 5)$ K and $T_m = (1128 \pm 9)$ K, respectively).

The Andersen thermostat [55] has been also included to adjust and tune the temperature, with collision frequency $5\,10^{11}$ s^{-1}. This value has been established based on the results of Ref. [41], where it was shown that a collision frequency of 10^{12} s^{-1} did not significantly alter the diffusive properties (velocity correlation function, diffusion coefficient) with respect to microcanonical simulations.

To evaluate the energy barrier of vacancy diffusion, the Drag Method (DM) is used. A vacancy is artificially created and fixed along a reaction coordinate (direction along which we want the vacancy to move), then the relaxation of the other $3N - 1$ (where N is the number of system atoms) degrees of freedom is carried out. By varying the fixed position, the profile of the vacancy diffusion barrier along the reaction coordinate is obtained. The value of the barrier is calculated as the difference between the top and bottom of the energy profile.

The geometric structure of the nanoalloys has been monitored by calculating Common Neighbour Analysis (CNA) signatures [56,57]. In the CNA, a signature consisting of three integer numbers (mnp) is associated to any pair of nearest-neighbour atoms: m is the number of common nearest neighbours of the pair, n is the number of nearest-neighbour bonds among the m common neighbours, and p is the maximum length of the chain which can be made with the n bonds. Here, two atoms are considered nearest-neighbour if they are separated by a distance shorter than 1.2 times the equilibrium interatomic distance in the bulk. Atoms along fivefold symmetry axes present the (555) signature with their neighbours, therefore this signature is very useful to detect transformations between fcc structures (no fivefold axes) and icosahedra (six fivefold axes). In this work, we have used the fraction of atomic pairs with (555) signature, that we have denoted as f_{555}. The (421) signature characterizes all nearest-neighbour pairs in bulk fcc crystals. The fraction f_{421} of (421) signatures has been used to track the evolution of fcc clusters.

Table 1
DFT-fitted [14] and EXP-fitted parameters [53].

		p	q	A (eV)	ξ (eV)	r_0 (Å)	r_{c1} (Å)	r_{c2} (Å)
DFT	Cu – Cu	10.6530	2.4900	0.092585	1.2437	1.28000	4.469094	5.160465
	Ni – Ni	11.7000	2.0450	0.096444	1.6111	1.24450	4.308652	4.975203
	Cu – Ni	11.1765	2.2675	0.104600	1.4453	1.26225	4.388873	5.067834
EXP	Cu – Cu	10.3770	2.6335	0.108400	1.3434	1.28000	3.62000	5.119450
	Ni – Ni	10.7630	2.4349	0.121700	1.6396	1.24450	3.52000	4.978030
	Cu – Ni	9.6999	2.9569	0.152900	1.6281	1.26225	3.62000	4.978030

Other quantities that have been calculated to track the evolution of the chemical ordering of CuNi nanoparticles are: the percentage of Cu atoms on the surface (s_{Cu}); the percentage of Cu−Cu bonds rescaled between the minimum and the maximum value (b_{Cu}).

Atomic-level pressure has been calculated from the atomic stress tensor [58–60], which, for each atom i in the nanoparticle, is defined as

$$\sigma_i^{ab} = \frac{1}{V_i} \sum_{j \neq j} \frac{\partial E_i}{\partial r_{ij}} \frac{r_{ij}^a r_{ij}^b}{r_{ij}}, \tag{5}$$

where E_i and V_i are the atomic energy of the ith atom and its volume in the bulk crystal structure, r_{ij}^a, r_{ij}^b (with $a, b = x, y, z$) and r_{ij} are the cartesian components and the length of the vector $\mathbf{r}_{ij}$ joining atoms i and j. The trace of the tensor is proportional to the isotropic local pressure on atom i:

$$P_i = -\frac{1}{3}\mathrm{Tr}(\underline{\sigma_i}). \tag{6}$$

Positive and negative values of P_i indicate compressive and tensile stress on atom i, respectively.

3. Assessment of the models on equilibrium properties

A preliminary study has been carried out on the two potential parameter sets in Table 1, in order to assess their validity against data in the literature. To this end, we have first calculated the enthalpy of mixing H^{mix} in bulk alloys and then we have focused on the equilibrium chemical ordering of nanoparticles.

To determine H^{mix} of CuNi, MC simulations have been performed in isothermal–isobaric ensemble on the bulk system. Simulations have been performed at 973 K, a temperature which is chosen to allow comparison with the data in the literature (see Fig. 1(a)). The enthalpy of mixing at a generic composition Cu_xNi_{1-x} is calculated as

$$H^{mix}_{Cu_xNi_{1-x}} = H_{Cu_xNi_{1-x}} - \left(x\, H_{Cu} + (1-x)\, H_{Ni}\right), \tag{7}$$

where $H_{Cu_xNi_{1-x}}$, H_{Cu} and H_{Ni} are enthalpies per atom. From Fig. 1(a) we observe that the CuNi system described by the DFT-fitted parameter set greatly overestimates the mixing enthalpy compared with the CALPHAD [61,62] data, because the DFT calculations overestimate the dissolution energy of isolated impurities, which were used to fit the potential in Ref. [14]. On the contrary, the EXP-fitted parameter set slightly underestimates the mixing enthalpy. The EXP-fitted set gives the correct asymmetry of the mixing enthalpy curve, with the maximum in the nickel-rich region.

To compare the results of the two sets at the nanoscale, MC simulations in the canonical ensemble have been performed using a truncated octahedral (TO) $Cu_{446}Ni_{140}$ nanoalloy. For both parameter sets and all simulation temperatures, in the equilibrium configurations almost all nickel atoms are arranged in the central region of the cluster, and surrounded by copper atoms on the surface.

In Fig. 1(b) the ratio of CuNi bonds is shown. The DFT-fitted set gives an increment of mixed bonds with increasing temperature, while for the EXP-fitted parameter set the ratio is almost constant. For the DFT-fitted set, as it is also shown in Figs. 1(c) and (d), there is a sharp phase separation between copper and nickel at low temperatures. Increasing the temperature, the degree of mixing increases, leading to a smooth transition from phase-separated to intermixed equilibrium configurations. On the contrary, using the EXP-fitted set, we observe an intermixed phase already at low temperatures (100 K) (see Figs. 1(e) and (f)).

The Ni-rich composition ($Cu_{140}Ni_{446}$) has also been tested. In the equilibrium configurations all Cu atoms are in surface sites (especially at vertices and edges). Since the number of Cu atoms is not sufficient to fill all surface sites, Ni atoms occupy some of them.

In summary, at equilibrium Cu atoms tend to occupy the surface sites while Ni atoms occupy the inner sites of CuNi nanoalloys. The two parameter sets behave differently, as the copper and nickel modelled by the DFT-fitted set present a greater tendency to phase separation compared to what happens with the EXP-fitted set. These results at the nanoscale are in agreement with what observed for the mixing enthalpies.

Given all the issues analysed above, we have chosen to use the EXP-fitted parameter set for the most part of the following calculations, because it seems to give a better description of the mixing behaviour between Cu and Ni. However, we will also show some results of the DFT-fitted set for comparison.

Finally, we have simulated the melting of the nanoalloys starting from configurations with optimized chemical ordering, in order to check the temperature range in which they are solid. We have considered four different structures, as shown in Fig. 1(g-j): icosahedron with 147 atoms (Ih_{147}), and truncated octahedra with 201 (TO_{201}), 586 (TO_{586}) and 976 atoms (TO_{976}). The compositions are $Cu_{13}Ni_{134}$, $Cu_{19}Ni_{182}$, $Cu_{140}Ni_{446}$ and $Cu_{140}Ni_{836}$, respectively. These sizes and compositions are those that will be treated in the following to study evolution from non-equilibrium Cu@Ni configurations. The sizes of our clusters are sufficiently small so that there is still competition between icosahedra, decahedra and crystalline structures, so that structural transformation may occur. Moreover, in this size range time scales of several microseconds in the simulations can be reached.

In all optimal chemical ordering configurations, Cu atoms occupy surface sites. However, their number is not sufficient to fill all surface sites, so that also Ni atoms are visible on the surface. In the melting simulations, we have started from low temperature and heated the cluster with heating rate $r_h = 1$ K/ns by molecular dynamics. The icosahedron melts at 970 ± 30 K, while the truncated octahedra TO_{201}, TO_{586} and TO_{976} melt respectively at 939±9 K, 1032±6 K and 1156±6 K.

4. Results

The objective of this paper is to study the evolution towards equilibrium of CuNi nanoalloys which are initially prepared in out-of-equilibrium configurations, i.e. with Cu@Ni core@shell arrangement. We have considered nanoalloys of different sizes and geometric structure, making two types of molecular dynamics simulations: heating and evolution at constant temperature. The behaviour of the nanoalloys has been characterized by monitoring f_{555}, f_{421}, s_{Cu} and b_{Cu}.

4.1. Heating simulations

In the MD heating simulations, the nanoalloys have been started at relatively low temperature in their solid state and heated up at a constant rate r_h until they have melted. In principle, heating may

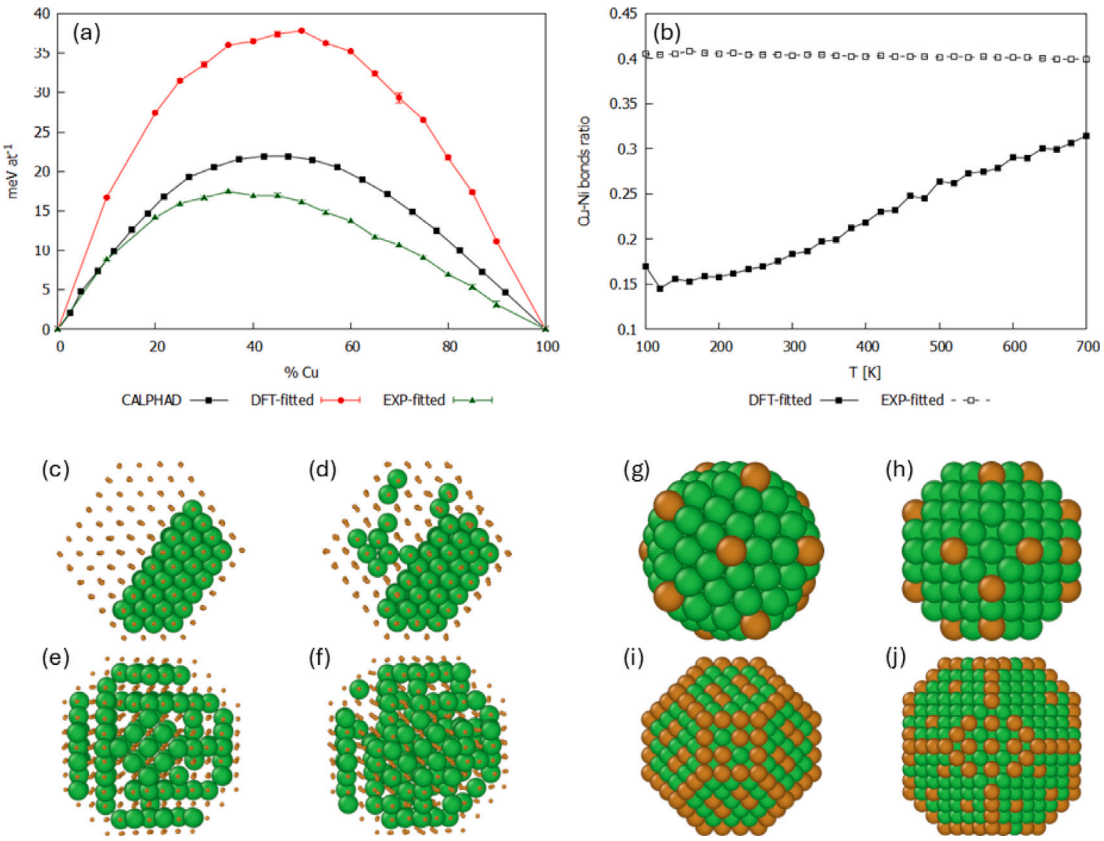

Fig. 1. Equilibrium properties of CuNi. (a) Mixing enthalpies for CuNi bulk system at 973 K calculated using the DFT- and EXP-fitted potentials and compared to CALPHAD data from Ref. [10]. (b) Fraction of CuNi nearest-neighbour bonds as a function of T for the TO $Cu_{446}Ni_{140}$ for both potentials. (c-d) Images of the nanoalloys from Monte Carlo simulations using the DFT-fitted set: (c) $T = 100$ K, (d) $T = 300$ K. (e-f) Images of the nanoalloys from Monte Carlo simulations using the EXP-fitted set: (e) $T = 100$ K, (f) $T = 300$ K. (g-j) Configurations with optimal chemical ordering obtained using the EXP-fitted set: (g) Ih $Cu_{13}Ni_{134}$, (h) TO $Cu_{19}Ni_{182}$, (i) TO $Cu_{140}Ni_{446}$, (j) TO $Cu_{140}Ni_{836}$. In all images, Cu and Ni atoms are represented by dark orange and green spheres, respectively.

induce also solid–solid structural transformations [63] at temperatures well below melting, especially if the initial configuration is strongly out of equilibrium. The results are shown in Fig. 2 and Table 2 for small nanoalloys (Ih_{147} and TO_{201}) and in Fig. 3 for larger ones (TO_{586} and TO_{976}).

For the icosahedron Ih_{147}, the initial structure is $Cu_{13}@Ni_{134}$, in which the Cu atoms occupy the central site and its twelve nearest neighbours. The TO_{201} starts with the arrangement $Cu_{19}@Ni_{182}$, where Cu atoms form a small octahedron at the centre of the cluster. For the TO_{586} and the TO_{976}, the initial configurations are $Cu_{140}@Ni_{446}$ and $Cu_{140}@Ni_{836}$, respectively with Cu atoms forming a centred TO core. In all cases, chemical ordering is opposite to the optimal one, in which Cu atoms are on the surface (see Fig. 1(g,h)). We have used three heating rates (r_h = 0.1, 1, 10 K/ns) running five independent simulations for each heating rate and structure.

In general, Cu atoms can reach the surface in two ways: either detaching from the core one by one or by processes in which several Cu atoms suddenly move together from the core to the surface. The one-by-one processes take place while the structure preserves its initial shape (bar small readjustments) while the multi-atom precesses require deep structural transformations [7,8], such as solid–solid transitions [63] and melting.

In Fig. 2(a-e) we show a representative simulation of the evolution of the Ih_{147}, where both processes can be observed. Four Cu atoms reach the surface at T = 874 K, followed by one atom at about 910 K and finally by the remaining eight Cu atoms at 926 K. This last process is associated to disordering of the geometric structure, which stays liquid-like for a few degrees (note that r_h = 1 K/ns in this case) before solidifying again in icosahedral shape at 934 K. The complete melting is achieved at about 960 K (see also Table 2). Liquid-like disordering and melting correspond to the increase of f_{555} from 0.05, which is the value for an icosahedron of this size, to about 0.1.

In Fig. 2(f-j) we show a simulation of the TO_{201}. For $800 < T < 840$ K, three Cu atoms reach the surface one by one while the structure keeps its TO shape. Just above 840 K, there is a sudden transition in which 14 Cu atoms suddenly reach the surface. At the same time, the cluster heavily disorders and then solidify into an incomplete Ih (see the jump of f_{555}). Finally, the remaining two Cu atoms reach the surface one by one well before melting.

While the Ih_{147} only changes its chemical ordering, the TO_{201} also changes its geometric structure, towards defective icosahedral or decahedral structures, which are lower in energy, by 0.38 and 0.55 eV, respectively. Cu diffusion within the TO_{201} depends on r_h. For r_h = 10 K/ns, very few Cu atoms reach the surface before the structural transformation, while for the slower rates, more Cu atoms reach the surface before the change in structure.

For the TO_{586} and TO_{976} we have never observed structural transformations into icosahedra or decahedra. Therefore we have monitored f_{421} instead of f_{555}. Results from representative simulations at r_h = 1 K/ns are shown in Fig. 3. In these simulations, the structure evolves without significant structural changes, with the exception of a certain disordering of the surface corresponding to a small decrease in f_{421}. Cu atoms reach the surface one by one until the cluster melts. At melting, all Cu atoms are ejected on the surface. The behaviour depends on r_h: the slower r_h, the larger number of Cu atoms reach the surface before melting (see also Table 3).

To obtain more quantitative information, we have considered the temperatures of a few characteristic events: melting (T_m); first detachment of a Cu atom from the core (T_d); arrival of the first Cu atom on

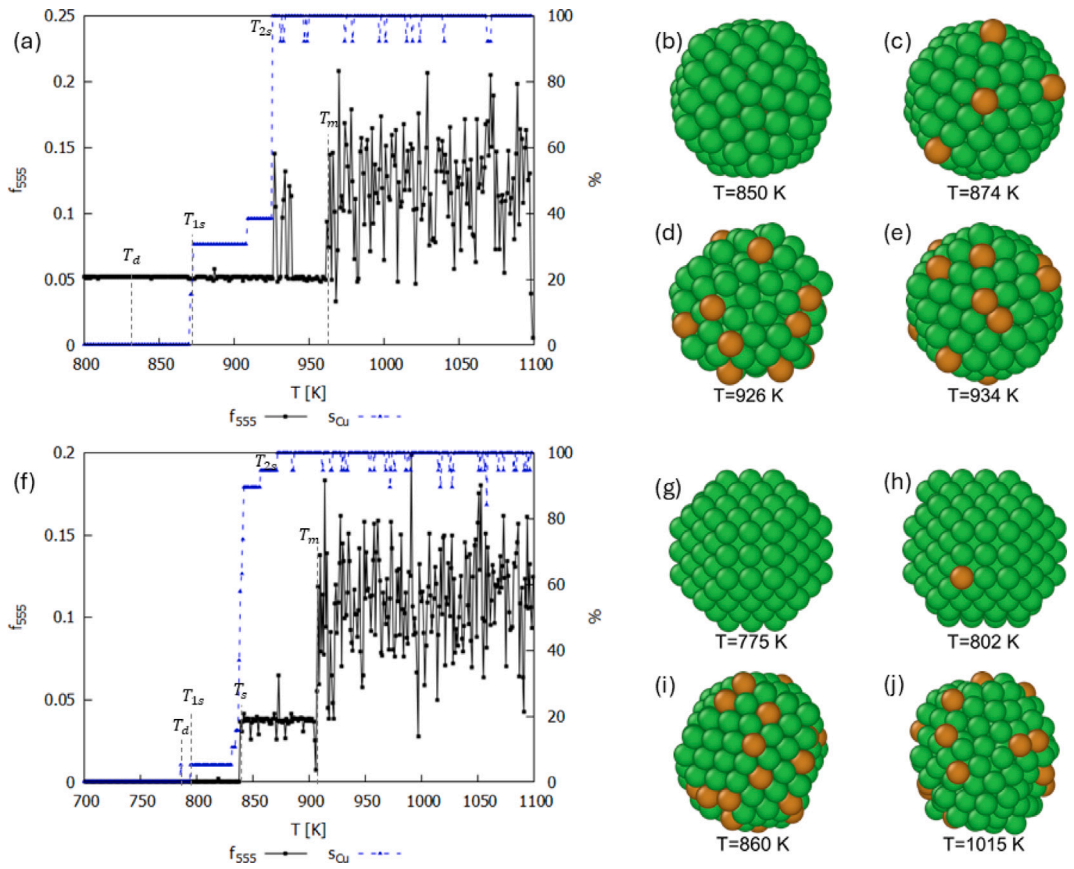

Fig. 2. Results of heating simulations: (a-e) Ih_{147}, (f-j) TO_{201}. In (a) and (f) we report f_{555} and s_{Cu} as functions of temperature T. The data are taken from representative simulations with heating rate $r_h = 1$ K/ns. In (b-e) and (g-j) we show snapshots from the simulations at different temperatures. In all images, Cu and Ni atoms are represented by dark orange and green spheres, respectively.

Table 2
(a) Melting temperatures T_m obtained in simulations with different heating rates r_h for Ih_{147}, TO_{201}, TO_{586} and TO_{976} structures. (b) Characteristic temperatures T_d, T_s, T_{1s} and T_{2s} obtained in simulations with $r_h = 0.1$ K/ns. All results are averaged over five independent simulations. Errors are calculated as standard deviations on the distributions of the different quantities.

	(a) Melting temperature T_m [K]			(b) Characteristic temperatures [K]			
	0.1 K/ns	1 K/ns	10 K/ns	T_d	T_s	T_{1s}	T_{2s}
Ih_{147}	990 ± 6	964 ± 12	969 ± 25	838 ± 17	–	838 ± 17	895 ± 16
TO_{201}	923 ± 4	928 ± 7	924 ± 11	788 ± 19	818 ± 12	788 ± 19	850 ± 14
TO_{586}	1024 ± 7	1022 ± 10	1042 ± 20	831 ± 14	–	833 ± 12	1008 ± 17
TO_{976}	1148 ± 8	1143 ± 5	1167 ± 6	896 ± 47	–	1008 ± 15	1145 ± 5

the surface (T_{1s}); convergence of the number of Cu atoms on the surface (T_{2s}); structural transformation (T_s, only for the TO_{201}). The results are reported in Table 2. T_m is reported for all r_h, which give compatible results. Even though the TO_{201} is larger than the Ih_{147}, its T_m is lower because of the strong stability of the icosahedron at the magic number 147. In the smaller clusters, T_d and T_{1s} essentially coincide, showing that once a Cu atom leaves the core, it reaches the surface very quickly. For the TO_{586} and TO_{976}, T_{1s} is slightly higher than T_d, because the detached Cu atom needs to cross a larger distance to arrive on the surface.

As a further analysis, we have characterized the diffusion and arrival of Cu atoms on the nanoparticle surface for all the different sizes and geometries, before the melting of the structure. In Table 3(a) we report the average percentage of Cu atoms that have reached the nanoparticle surface before melting. Specifically, we have considered those atoms reaching the surface from the beginning of the heating simulation to a temperature corresponding to the 95% of T_m. Our data show clear trends with size and heating rate. The percentage of Cu atoms on the surface increases by slowing the heating process; in the smallest structures, most Cu atoms are able to reach the surface well below the melting temperature. In Table 3(b), we report the percentage of Cu atoms on the surface before melting (i.e. those considered in Table 3(a)) that arrived by one-by-one diffusion processes. In this case, the trends are less evident, though there is some indication that one-by-one diffusion becomes more important with increasing size.

To further check the sensitivity to core size and shell thickness, we have considered a TO_{976} with bigger Cu core ($Cu_{314}@Ni_{662}$). We have performed five independent simulations, heating the clusters at 1 K/ns. The average temperature of detachment of the first Cu atom $T_d = (892 \pm 24)$ K, which in this case is almost coincident with T_{1s}, due to the reduced thickness of the shell. This behaviour is qualitatively the same as found for the TO_{586} with initial configuration $Cu_{140}@Ni_{446}$, since the two clusters have the same shell thickness.

For comparison, we have also considered the Ni@Cu case. Specifically, we have simulated the melting of a TO_{586}, with initial configuration $Ni_{140}@Cu_{446}$. We have made five independent simulations, finding that the melting temperature is (845 ± 24) K. The Ni core slowly dissolves as the temperature increases, but, at variance with the Cu@Ni

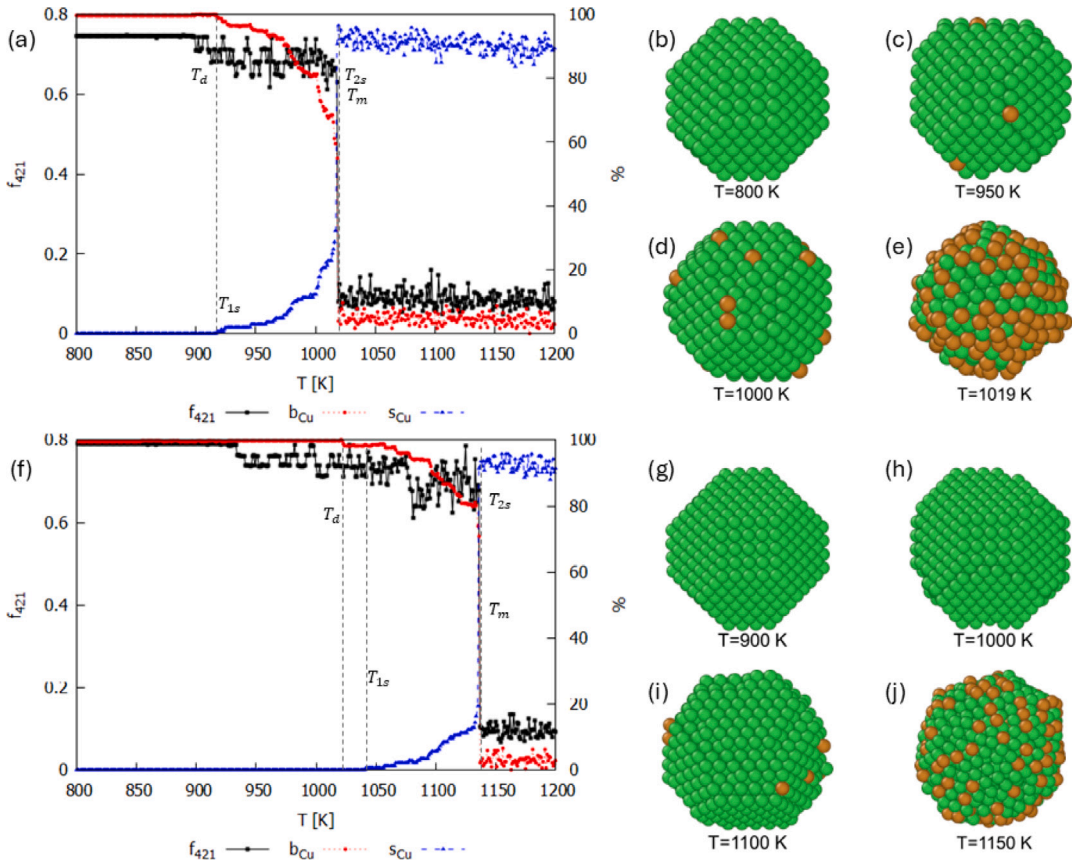

Fig. 3. Results of heating simulations for (a-e) TO_{586} and for (f-j) TO_{976} with $r_h = 1$ K/ns. (a) and (f): f_{421}, b_{Cu} and s_{Cu} as functions of temperature T. (b-e): snapshots from simulations of the TO_{586}. (g-j): snapshots from simulations of the TO_{976}. The temperatures of the snapshots are reported below the images. Cu and Ni atoms are represented by dark orange and green spheres, respectively.

Table 3
(a) Percentage of Cu atoms reaching the surface of the nanoparticle before melting (see the text for more details). (b) Percentage of Cu surface atoms (i.e. those considered in (a)) arrived on the surface by one-by-one diffusion. All results are averaged over five independent simulations. Errors are calculated as standard deviations on the distributions of the different quantities.

	(a) Cu on the surface before melting [%]		(b) One-by-one diffusion [%]	
	0.1 K/ns	1 K/ns	0.1 K/ns	1 K/ns
Ih_{147}	100 ± 0	60 ± 37	63 ± 7	63 ± 25
TO_{201}	100 ± 0	99 ± 2	68 ± 10	42 ± 18
TO_{586}	59 ± 23	11 ± 7	66 ± 7	84 ± 15
TO_{976}	20 ± 7	1 ± 1	81 ± 8	100 ± 0

case, Ni atoms do not reach the surface but remain in the internal part of the cluster, so that the composition of the surface does not significantly change. This behaviour is as expected, since at sufficiently high temperatures the two metals are miscible, but there is a preference of Cu atoms to occupy surface sites. No geometric transformations have been observed.

4.2. Diffusion at constant temperature

To better characterize the diffusion of Cu atoms, we have simulated the evolution of the Cu@Ni TO_{586} and TO_{976} at constant temperature (below the melting range) for 1 μs. For the TO_{586}, 950, 975 and 1000 K have been chosen, whereas for the TO_{976}, 1050, 1075 and 1100 K have been selected.

We have observed the same behaviour for both sizes. The core gradually dissolves as Cu atoms diffuse one by one to the surface, as shown by the rather regular increase of s_{Cu} of Fig. 4(a,b), while the nanoalloys mostly preserve the TO shape, albeit with some defects. Cu atoms reach the surface of the TO_{976} more slowly, because they have to cross one more Ni layer than in the TO_{586}.

However, there is an exception to this behaviour, which regards the TO_{586} at 1000 K. In this case, s_{Cu} increases very quickly in the initial stages of the simulations, indicating a quick diffusion of copper in the early nanoseconds of evolution. To better characterize this behaviour, in Fig. 4(c) we report s_{Cu} and f_{421} in logarithmic scale. In the very first ns, Cu atoms reach the surface one by one, up to a fraction of about 20%. Then there is a sudden jump in s_{Cu}, here occurring at about $t = 7$ ns, which indicates that almost all the remaining Cu atoms leave the core and reach the surface in a very short time interval. This event can be well understood by inspecting the behaviour of f_{421}, which is reported in Fig. 4(c). The sudden increase of s_{Cu} occurs simultaneously with the fall of f_{421} to values typical of a liquid droplet. The cluster keeps a liquid-like structure for about 25 ns and then solidifies into a TO structure with some defects, such as islands in hcp stacking. The evolution of the cluster is also shown in the simulation snapshots of Fig. 4(d-g). This type of behaviour, with a clear transition to a liquid-like state followed by solidification, has been observed in 8 of 10

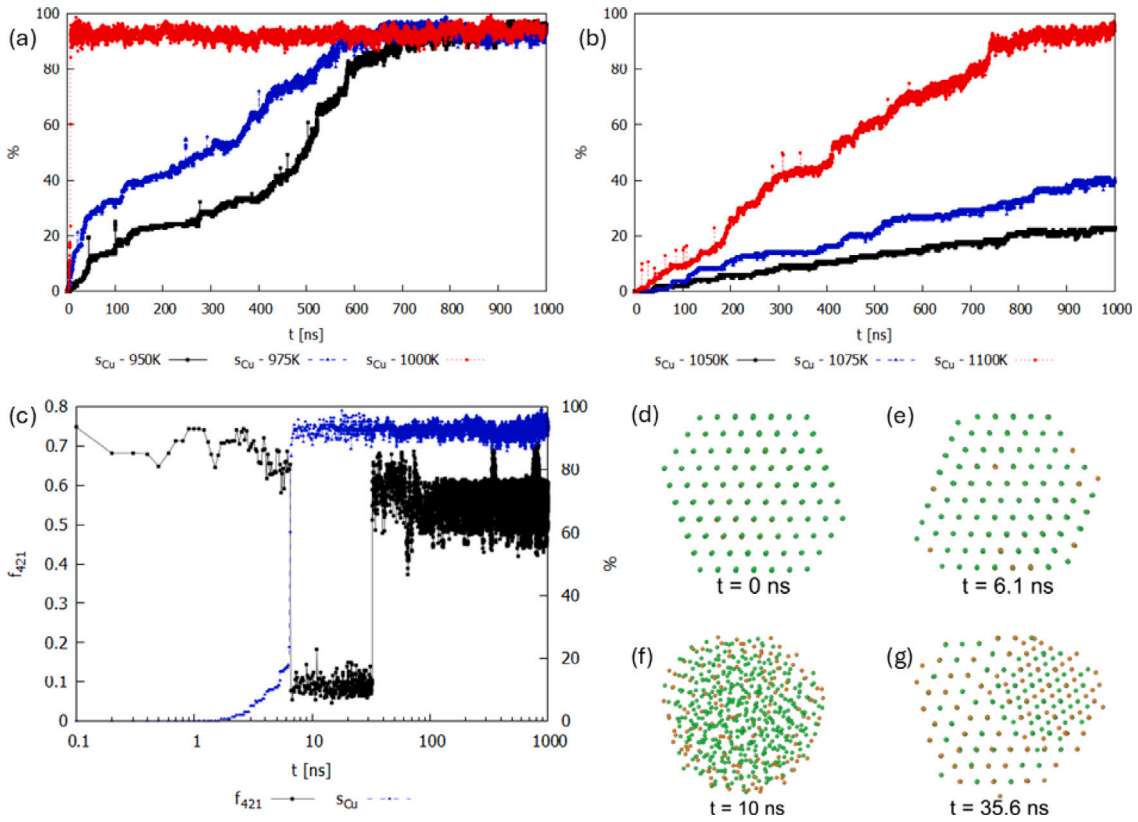

Fig. 4. Results of 1 μs MD simulations at constant temperature for (a, c–g) TO_{586} and for (b) TO_{976}. (a) Percentage of Cu atoms on surface of TO_{586} for simulations at 950 K, 975 K, 1000 K. (b) Percentage of Cu atoms on surface of TO_{976} for simulations at 1050 K, 1075 K, 1100 K. (c) s_{Cu} and f_{421} for the TO_{586} from a typical simulation at 1000 K. (d–g) Snapshots from the same simulation as in (c) at different times. The structures in (d) and (e) are perfect TO, while the structures in (f) and (g) are liquid-like and defective TO, respectively. All structures in the snapshots are locally minimized to eliminate the effect of vibrations.

independent simulations at 1000 K. Although the qualitative behaviour is the same in all 8 simulations, the transformation begins at different times, in a range between 7 and 160 ns, and the duration of the liquid phase is quite variable, from a few nanoseconds to more than a hundred.

4.3. Vacancy formation and vacancy-mediated diffusion

Here we analyse the elementary mechanisms of Cu atom diffusion. We focus on the first diffusion event of a Cu atom detaching from the core of the TO_{586} (Cu_{140}@Ni_{446}). The Cu core is a small TO with 2 × 2 square (100) facets and irregular hexagonal (111) facets. There are 96 Cu atoms at the interface with Ni – 24 Cu atoms in (100) facets, 24 atoms in edges between (111) facets and 48 atoms in the central part of (111) facets. We have performed 75 constant temperature simulations for each temperature (925, 950, 975 and 1000 K), collecting data every ps. In all simulations, we have looked at the first detachment of a Cu atom from the core and analysed the atomic-level mechanism of the diffusion event. The behaviour of the TO_{976} is very similar, and therefore we will not describe it in detail.

As shown in Fig. 5(a), the first atom detaches from a (100) facet in about 80% of the cases. In the remaining cases, it detaches from edges between (111) facets, with the exception of the highest temperature, at which there is a non negligible percentage of detachments from (111) facets. Along with the detachment of the Cu atom, we have detected very often (see Fig. 5(b)) the formation of a vacancy in the Cu core at the interface with the Ni shell. The vacancy is refilled after some time, which tends to be shorter with increasing temperature. Fewer vacancies have been observed at the highest temperature because their average lifetime becomes so short to probably escape our sampling interval of 1 ps.

The preferential detachment of Cu atoms from (100) facets is notable, because only 24 of the 96 Cu atoms at the interface with Ni are in these facets. To understand why this happens, we have calculated the atomic-level pressure in the initial configuration. The pressure map of the initial configuration is reported in Fig. 6. All Cu atoms at the interface with Ni are somewhat compressed (positive pressure), because of Laplace pressure and of the larger atomic size of Cu compared to Ni [59]. Atoms in (100) facets are the most compressed, followed by those in the edges between (111) facets and finally by those in the central part of (111) facets. This map therefore correlates very well with the probability of the site from which the first Cu atom detaches.

4.3.1. Vacancy formation, diffusion and filling

The formation of a vacancy occurs by sequences of several events, as the one shown in Fig. 7(a-g). Although being a complex sequence, it lasts a few ps. The process starts at the surface of the nanoparticle, where some Ni atoms move on the surface (medium size blue spheres in the figure). These displacements create surface defects in correspondence of a (100) facet. At this point, a chain of a few Ni atoms and one Cu atom moves by one lattice step towards the surface of the cluster. The Cu atom leaves a vacancy in the surface of the core. In the case shown here, the vacancy persists for 3 ps before being filled again by a Ni atom. The filling process, shown in Fig. 7(g,h), involves two Ni atoms moving from the outside to the inside of the cluster. In this way, the diffusion of the Cu atom is completed. Similar diffusion processes have been found in TO_{976} (see Fig. 8). The main difference is that the displacement of the Cu atom from the core surface involves a longer chain of Ni atoms because of the increased thickness of the Ni shell. Similar chain mechanisms have been observed in the diffusion of impurities in icosahedral clusters [48].

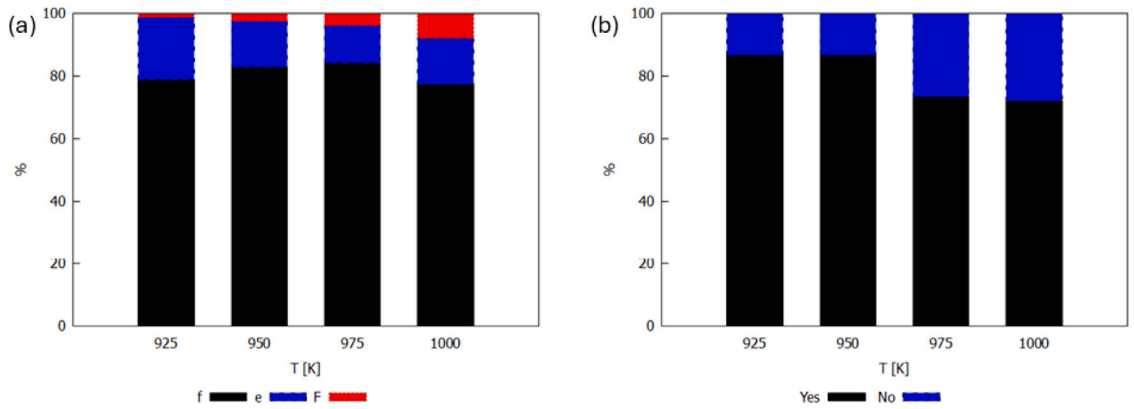

Fig. 5. First detachment event of a Cu atom from the core of the TO_{586} at $T = 925$, 950, 975 and 1000 K. (a) Percentage of Cu atom detachment events from the positions: (100) facet (f), edge (e) and (111) facet (F). (b) Percentage of diffusion events of a Cu atom, specifying whether a vacancy is formed (Yes) or not (No).

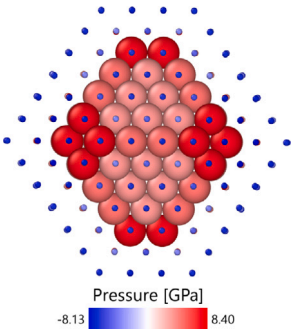

Fig. 6. Pressure map of the initial configuration $Cu_{140}@Ni_{446}$. Cu and Ni atoms are represented by large and small spheres, respectively. Red atoms are at positive pressure.

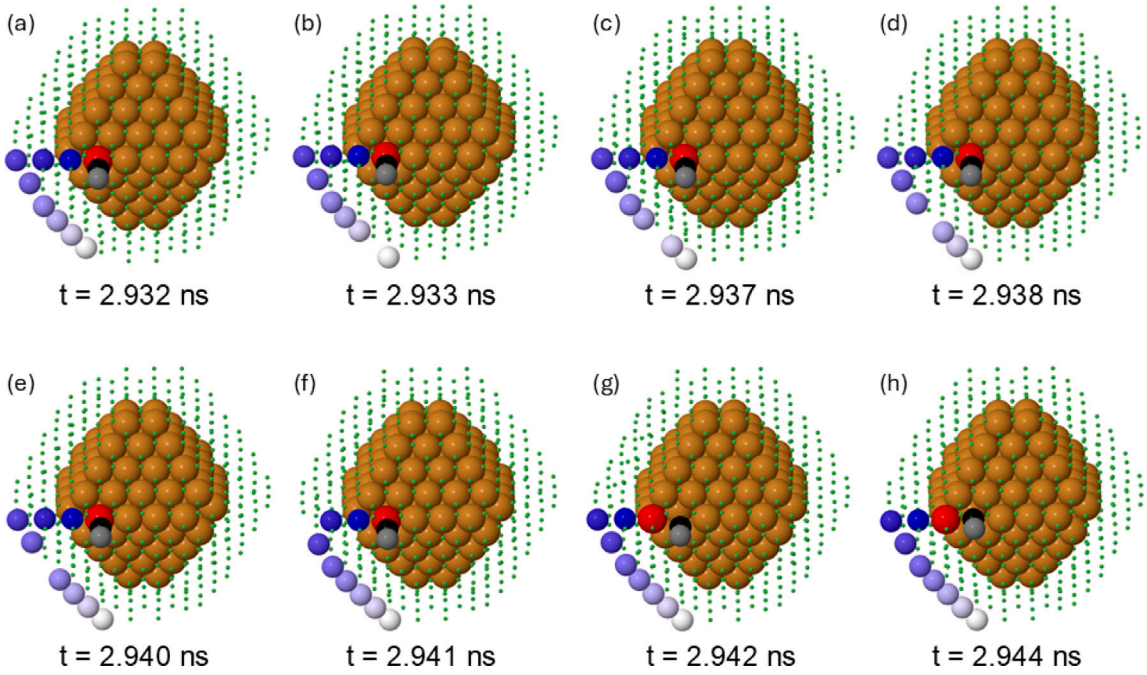

Fig. 7. Vacancy creation and occupation process in the TO_{586}. Cu atoms: large spheres. Ni atoms: medium and small spheres. The atoms not involved in the process are coloured in dark orange (Cu) and green (Ni). The atoms involved in the process are coloured in red (Cu) and shades of blue and grey (Ni). The red copper atom leaves a vacancy on the core surface, the blue-scale nickel atoms move upon vacancy creation whereas the grey-scale ones are involved in the filling process.

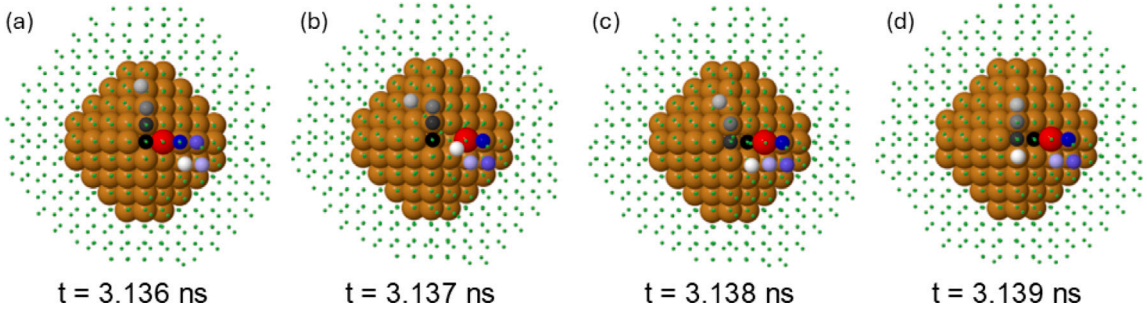

Fig. 8. Vacancy creation and occupation process in the TO_{976}. Cu atoms: large spheres. Ni atoms: medium and small spheres. The atoms not involved in the process are coloured in dark orange (Cu) and green (Ni). The atoms involved in the process are coloured in red (Cu) and shades of blue and grey (Ni). The red copper atom leaves a vacancy on the core surface, the blue-scale nickel atoms move upon vacancy creation whereas the grey-scale ones are involved in the filling process.

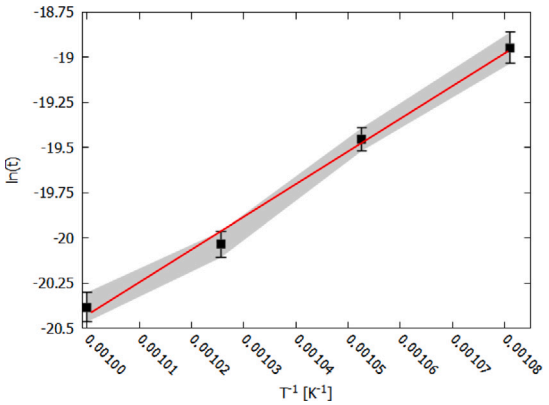

Fig. 9. Arrhenius plot of the average time $\bar{t}$ for the first displacement of a Cu atom from the core. The black dots show $\ln \bar{t}$ ($\bar{t}$ in s), where $\bar{t}$ is the average over 75 events of first Cu atom detachment from the core, as function of T^{-1}. The red line is the resulting fit of the data.

To estimate the energy barrier for vacancy formation on the surface of the Cu core, we have made the Arrhenius plot of the average time $\bar{t}$ needed for the appearance of the first vacancy. We note that this barrier arises from the combination of a complex collection of processes, as it includes the contributions of many different chain mechanisms, starting from all different positions in the core; moreover, for each starting position, several different chain-type displacements are possible. To calculate $\bar{t}$, we have collected the waiting time for the first appearance of a vacancy in 75 independent simulations for each temperature. The distribution of the collected waiting times is not a pure exponential, which is a clear indication of the combination of different possible processes. Anyway, we have checked whether the temperature dependence of $\bar{t}$ can still be fitted by the Arrhenius law, which reads

$$\bar{t} = A \exp\left(\frac{E_f}{k_B T}\right), \tag{8}$$

where A is the time prefactor and E_f is the barrier for vacancy formation. The fit is reasonable (see Fig. 9) and gives $E_f = (1.56 \pm 0.09)$ eV and $A = (2 \pm 2)\ 10^{-17}$ s. The time prefactor is very small since it corresponds to a very large frequency prefactor of 10^{16-17} s^{-1}. Such prefactors are common to collective events involving the concerted displacement of several atoms [48,64].

The value of E_f cannot be directly compared to experimental results in the literature, because the latter only refer to pure Cu and Ni bulk crystals and report the energy ΔE_f (not the barrier) for vacancy formation. In particular $\Delta E_f = (1.55 \pm 0.05)$ and (1.27 ± 0.05) eV for Ni and Cu, respectively [65,66]. Since the formation barrier must be larger than the formation energy, our result is consistent with experimental results.

In our simulations, we have also observed that the vacancy may be filled by the same Cu atom that has produced it, which returns in its original position. In this case, there is no net displacement of Cu atoms, as the cluster recovers its initial configuration.

4.3.2. Energy barriers for the diffusion of vacancies

So far, we have only analysed situations in which the vacancy, after being formed, is filled again in the same site where it was formed. However, there are cases in which the vacancy diffuses within the cluster before being filled. In our simulations, the vacancy usually moves along the edges or on the different sites of (100) facets of the core. In rare cases, the vacancy moves from the core surface towards its inner part, where it diffuses for some time but eventually reaches the CuNi interface again, where it is filled. In general, the lifetime of a vacancy decreases with temperature (2.8 ± 0.5) ps at $T = 925$ K to (1.12 ± 0.15) ps at $T = 1000$ K.

In most cases, the diffusion of a vacancy is caused by the displacement of a neighbouring atom which moves into the vacancy, freeing its starting site. The other neighbouring atoms make only small movements to better relax around the diffusing atom. Therefore, the diffusion process of a vacancy is much simpler than its formation and filling processes, because in diffusion only one atom is significantly displaced, instead of several atoms in a concerted way.

We have calculated the diffusion barrier E_d for a vacancy placed in different positions in the TO_{976}. We have considered single-element Cu and Ni nanoparticles and the Cu@Ni nanoalloy, and 9 different initial positions of the vacancy, as summarized in Fig. 10(a,b). The energy profile of some diffusion paths are represented in Fig. 10(c,d). The values of the barriers are reported in Table 4, for both the EXP-fitted and the DFT-fitted potentials.

Let us consider first the diffusion in pure Cu and Ni nanoparticles. We have analysed four initial positions (see Fig. 10(a)). Position 1 is at the centre of the nanoparticle, position 2 is somewhat closer to the

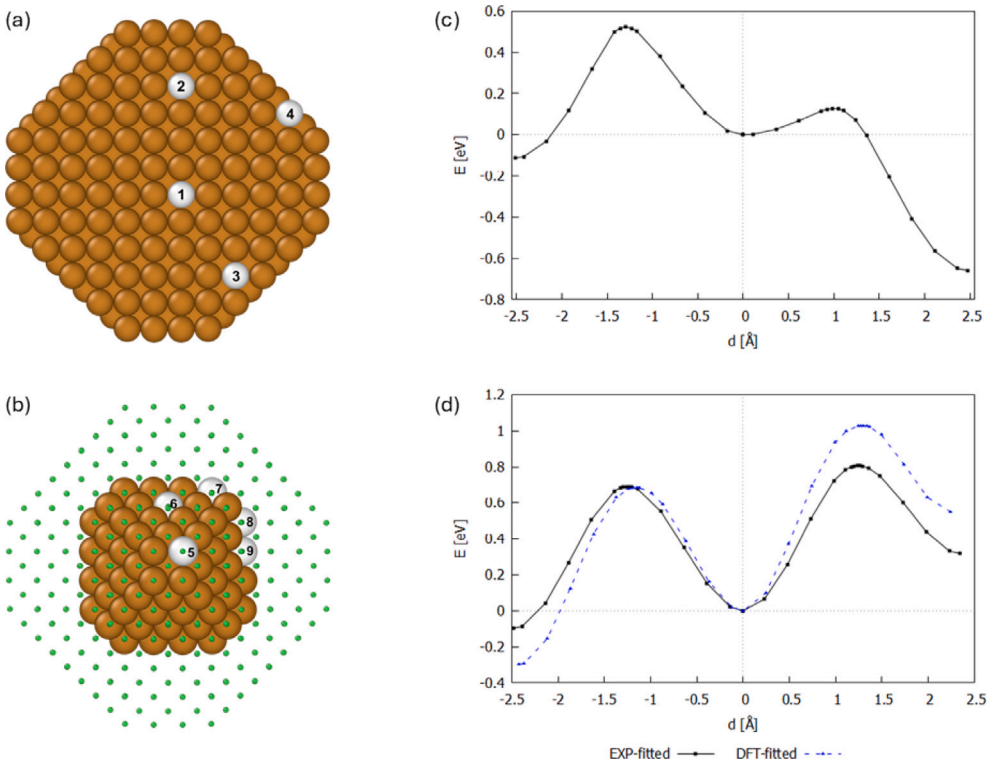

Fig. 10. (a, b) Initial vacancy position before the diffusion process. In the calculations, we considered only one vacancy at a time. Here we represent all of them in the same cluster. (a) Initial positions of the vacancies within the pure nanoparticles. (b) Initial positions of the vacancies within the core@shell Cu@Ni nanoparticle. (c) Energy profile for the diffusion of the vacancy in 'Position 3' in Cu nanoparticle, calculated with EXP-fitted potential. (d) Energy profile for the diffusion of the vacancy in 'Position 9', calculated with both sets of parameters. d is the distance of the vacancy from its initial position.

nanoparticle surface, position 3 is one layer below the surface and position 4 is on the surface. In positions 1,2 and 3, the vacancy can move to the left (L) and to the right (R), while in position 4 the only possible move is to the left. From the comparison of the barriers of positions 1,2 and 3 it turns out that the motion of the vacancy becomes progressively easier when approaching the nanoparticle surface. In particular, a vacancy in the subsurface position has to overcome a quite low barrier to reach the surface of the nanoparticle. Correspondingly, the barrier for displacing the vacancy from the surface position 4 to a neighbouring subsurface position is very high. In general, barriers in pure Ni are higher than in pure Cu, as expected because Ni is more cohesive. The DFT-fitted potential gives systematically higher barriers than the EXP-fitted potential, but the qualitative trends are the same.

In the literature, there are experimental results for migration energies of vacancies in pure bulk Ni and Cu crystals [66–70]. The experimental values are $E_d = 1.01$ [68], 1.05 [69] and 1.08 eV [70] for Ni, and (0.74 ± 0.08) eV for Cu. These values must be compared with the barriers for a vacancy located far from the nanoparticle surface, as in position 1. We have verified by calculations on larger TO structures, up to size 4033 atoms, that the value of the barrier of the process 1L is at convergence with respect to nanoparticle size, and therefore corresponds to the barrier in the bulk crystal. Specifically, we have calculated the barriers for TO clusters of sizes 1925, 2075 and 4033 for both metals and potential parametrizations, finding that the values are the same as found for the TO_{976}.

From the results in Table 4, it turns out that for Cu the DFT-fitted potential is in excellent agreement with the experimental result and the EXP-fitted potential slightly underestimates the barrier. For Ni, the DFT-fitted potential is again in excellent agreement with the experiment while the EXP-fitted potential underestimates the barrier by about 20%.

In the core@shell Cu@Ni nanoparticle, the vacancy has been initially placed on the core surface, at the copper-nickel interface, as at the beginning of the diffusive processes observed in the simulations. We have considered five initial positions (see Fig. 10(b)). The corresponding barriers for moving the vacancy to the left (L) and to the right (R) are reported in Table 4. The positions are: (100) facet (positions 5,7,8), centre of (111) facet (position 6), edge between (111) facets (position 9). Note that the initial positions 5, 7 and 8 are equivalent, but, due to their different placements with respect to the x axis, the L and R moves bring the vacancy to non-equivalent sites. The moves with lower barriers still

Table 4
Vacancy diffusion energy barriers E_d (in eV) for the different initial positions (see Fig. 10). Where possible, the vacancies are displaced both to the left (L) and to the right (R). In all cases, barriers are evaluated by EXP-fitted and DFT-fitted potentials.

Position	EXP-fitted		DFT-fitted	
	Cu	Ni	Cu	Ni
1L	0.65	0.84	0.73	1.11
1R	0.65	0.82	0.73	1.11
2L	0.58	0.74	0.66	1.03
2R	0.58	0.73	0.66	1.03
3L	0.52	0.65	0.64	0.99
3R	0.13	0.15	0.17	0.24
4	0.73	0.94	0.81	1.29
5L	0.88		1.11	
5R	1.12		1.55	
6L	0.63		0.77	
6R	0.63		0.77	
7L	0.61		0.73	
7R	0.78		1.07	
8L	0.65		0.66	
8R	0.81		1.05	
9L	0.69		0.69	
9R	0.81		1.03	

Table 5
Summary of vacancy migration energies in pure Cu, pure Ni and Cu@Ni nanoparticles. Experimental data for vacancy migration energies in the pure Cu and Ni bulk crystal are taken from [66] and [68–70], respectively. All values are in eV.

	Experimental data	EXP-fitted	DFT-fitted
Cu	0.74	0.65	0.73
Ni	1.01, 1.05, 1.08	0.84	1.12
Cu@Ni	–	0.61 – 1.12	0.69 – 1.55

keep the vacancy in the Cu core, either moving it on (111) facets (moves 6L, 6R), or along edges between (111) facets (7R), or displacing it inside the core (8L, 9L). The only high-barrier move that maintains the vacancy in the Cu core is the 5L move, in which the vacancy is shifted within a (100) facet. The moves that displace the vacancy from the Cu core to the Ni shell (5R, 7R, 8R, 9R) have high barriers, especially move 5R in which the vacancy is displaced on a (100) plane. Also for these diffusion processes the DFT-fitted potential gives higher barriers than the EXP-fitted potential, but the qualitative trends are the same. These results explain why in our MD simulations the vacancies do not migrate towards the cluster surface, but are confined to the NiCu interface. This result can also be interpreted in the light of the pressure map in Fig. 6: it reveals the preference for the vacancy to be located in sites under positive pressure, to relax the local compressive stress.

In Table 5 we report a summary of the vacancy diffusion energies obtained by both the EXP- and DFT-fitted parametrizations of the SMA-TB potential, and the experimental data in the literature, when available. Experimental data refer to macroscopic crystals, and are therefore compared to energy barriers for vacancy migration in the central sites of large Cu and Ni nanoparticles. For Cu@Ni nanoparticles, we report the range of values obtained for different vacancy migration processes at the Cu-Ni interface (complete data are reported in Table 4).

5. Conclusions

Cu@Ni nanoparticles in the gas phase are strongly out of equilibrium. Their evolution towards equilibrium causes Cu atoms to migrate towards the surface of the nanoparticle. Our simulations have shown that this migration can occur in different ways: Cu atoms can detach from the initial core one at a time and then reach the surface at different times by passing through the Ni shell; alternatively, the core can suddenly dissolve, at least in part, while a structural transformation takes place. In the latter case, in which several Cu atoms reach the surface almost simultaneously, the structural transformations comprise two stages. In the first stage, the nanoparticle disorders becoming liquid-like, and atoms in the nanoparticle diffuse very quickly, so that most Cu atoms can reach the surface. After some time, the nanoparticle solidifies again. The smallest fcc cluster (TO_{201}) solidifies into decahedral or icosahedral structures, that are more energetically favourable in this size range, whereas the larger fcc nanoparticles solidify again in the same fcc structure, albeit with some defects, such as stacking faults. The structural transformations from fcc to icosahedral or decahedral structures occurring in our simulations should be observable in experiments. Also the transitions to metastable liquid-like structures should be experimentally observable. For example, these types of transformations were already observed in Au clusters of comparable sizes [71].

The one-by-one migration of Cu atoms from the core to the surface tends to become dominant as the size of the nanoparticle increases. This type of process begins at the interface between the Cu core and the Ni shell, where a Cu atom detaches from the core (usually through a concerted multi-atom process) leaving a vacancy at the interface. The vacancy can be filled quickly or diffuse within the nanoparticle for some time before being filled. We have analysed the diffusion of an isolated vacancy, also considering the cases of pure Ni and Cu nanoparticles, for which experimental data on vacancy diffusion barriers in bulk systems are available. Our results have shown that vacancies become more mobile when they are located closer to the surface in pure Cu and Ni nanoparticles. The diffusion barriers for vacancies in central sites of larger nanoparticles agree very well with the experimental data on vacancy diffusion in bulk samples. For vacancies created at the interface between the Cu core and the Ni shell, mobility is preferentially along the interface or towards the inner core, while mobility towards the Ni shell is more difficult.

In summary, our simulations have shown that Cu@Ni nanoparticles are quite stable, as interdiffusion activates at temperatures relatively close to the melting point. This is true in the time scale of molecular dynamics, but it suggests that Cu@Ni configurations should have a long lifetime at room temperature. From our data, it is difficult to extrapolate the room temperature lifetime; however, we note that stability can be further enhanced by oxidation of the top layers of the Ni shell. In fact, copper diffusion in Cu@Ni nanowires was obtained after reduction to eliminate the oxide and local heating [31,40].

CRediT authorship contribution statement

Luca Benzi: Writing – review & editing, Writing – original draft, Validation, Software, Investigation. **Diana Nelli:** Writing – review & editing, Writing – original draft, Validation, Supervision, Methodology. **Christine Mottet:** Writing – review & editing, Writing – original draft, Validation, Methodology, Investigation. **Riccardo Ferrando:** Writing – review & editing, Writing – original draft, Validation, Supervision, Software, Project administration, Methodology, Funding acquisition.

Acknowledgements

The authors acknowledge financial support under the National Recovery and Resilience Plan (NRRP), Italy, Mission 4, Component 2, Investment 1.1, Call for tender No. 104 published on 2.2.2022 by the Italian Ministry of University and Research (MUR), funded by the European Union – NextGenerationEU– Project Title PINENUT – CUP D53D23002340006 - Grant Assignment Decree No. 957 adopted on 30/06/2023 by the Italian Ministry of University and Research (MUR). The authors acknowledge networking support from the IRN Nanoalloys of CNRS.

Declaration of competing interest

The authors declare that they have no known competing financial interests or personal relationships that could have appeared to influence the work reported in this paper.

References

[1] R. Ghosh Chaudhuri, S. Paria, Classes, properties, synthesis mechanisms, characterization, and applications, Chem. Rev. 112 (2012) 2373–2433, http://dx.doi.org/10.1021/cr100449n.
[2] R. Ferrando, J. Jellinek, R.L. Johnston, Nanoalloys: From theory to applications of alloy clusters and nanoparticles, Chem. Rev. (Washington, DC) 108 (2008) 845–910, http://dx.doi.org/10.1021/cr040090g.
[3] M.B. Gawande, A. Goswami, T. Asefa, H. Guo, A.V. Biradar, D.-L. Peng, R. Zboril, R.S. Varma, Core–shell nanoparticles: synthesis and applications in catalysis and electrocatalysis, Chem. Soc. Rev. 44 (2015) 7540–7590, http://dx.doi.org/10.1039/C5CS00343A.
[4] V. Coviello, D. Forrer, V. Amendola, Recent developments in plasmonic alloy nanoparticles: Synthesis, modelling, properties and applications, ChemPhysChem 23 (2022) e202200136, http://dx.doi.org/10.1002/cphc.202200136.
[5] Y. Zou, Z. Sun, Q. Wang, Y. Ju, N. Sun, Q. Yue, Y. Deng, S. Liu, S. Yang, Z. Wang, F. Li, Y. Hou, C. Deng, D. Ling, Y. Deng, Core–shell magnetic particles: Tailored synthesis and applications, Chem. Rev. 125 (2025) 972–1048, http://dx.doi.org/10.1021/acs.chemrev.4c00710.
[6] R. Ferrando, Structure and properties of nanoalloys, in: Frontiers of Nanoscience, vol. 10, Elsevier, 2016.

[7] D. Nelli, R. Ferrando, Core-shell. vs, Multi-shell formation in nanoalloy evolution from disordered configurations, Nanoscale 11 (2019) 13040–13050.

[8] D. Nelli, C. Mottet, R. Ferrando, Interplay between interdiffusion and shape transformations in nanoalloys evolving from core–shell to intermixed structures, Faraday Discuss. 242 (2023) 52–68, http://dx.doi.org/10.1039/D2FD00113F.

[9] M.A. Turchanin, P.G. Agraval, A.R. Abdulov, Phase equilibria and thermodynamics of binary copper systems with 3d-metals. vi. copper-nickel system, Powder Met. Met. Ceram. 46 (2007) 467–477, http://dx.doi.org/10.1007/s11106-007-0073-x.

[10] M. Hennes, J. Buchwald, S. Mayr, Structural properties of spherical cu/ni nanoparticles, CrystEngComm 14 (22) (2012) 7633–7638.

[11] W. Tyson, W. Miller, Surface free energies of solid metals: Estimation from liquid surface tension measurements, Surf. Sci. 62 (1977) 267–276, http://dx.doi.org/10.1016/0039-6028(77)90442-3.

[12] C. Kittel, Introduction To Solid State Physics, University of California, Berkeley, 2005.

[13] H. Brongersma, M. Sparnaay, T. Buck, Surface segregation in cu-ni and cu-pt alloys; a comparison of low-energy ion-scattering results with theory, Surf. Sci. 71 (1978) 657–678, http://dx.doi.org/10.1016/0039-6028(78)90453-3.

[14] E. Panizon, J.A. Olmos-Asar, M. Peressi, R. Ferrando, Study of structures and thermodynamics of cuni nanoalloys using a new dft-fitted atomistic potential, Phys. Chem. Chem. Phys. 17 (2015) 28068–28075, http://dx.doi.org/10.1039/C5CP00215J.

[15] V. Romanovski, N. Sdobnyakov, S. Roslyakov, A. Kolosov, K. Podbolotov, K. Savina, W. Kwapinski, D. Moskovskikh, A. Khort, Bimetallic cuni nanoparticle formation: Solution combustion synthesis and molecular dynamic approaches, Inorg. Chem. 63 (2024) 24844–24854, http://dx.doi.org/10.1021/acs.inorgchem.4c04260.

[16] N. Sdobnyakov, A. Khort, V. Myasnichenko, K. Podbolotov, E. Romanovskaia, A. Kolosov, D. Sokolov, V. Romanovski, Solution combustion synthesis and monte carlo simulation of the formation of cuni integrated nanoparticles, Comput. Mater. Sci. 184 (2020) 109936, http://dx.doi.org/10.1016/j.commatsci.2020.109936.

[17] Y. Sun, S. Liu, X. Guo, S. Huang, Structural, Magnetic and electronic properties of $cu_n ni_{55-n}$ ($n = 0 - 55$), Comput. Theor. Chem. 1154 (2019) 11–16, http://dx.doi.org/10.1016/j.comptc.2019.03.008.

[18] Q. Wang, X. Wang, J. Liu, Y. Yang, Cu–ni core–shell nanoparticles: structure, stability, electronic, and magnetic properties: a spin-polarized density functional study, J. Nanoparticle Res. 19 (2017) 25, http://dx.doi.org/10.1007/s11051-016-3731-4.

[19] L. Pielsticker, I. Zegkinoglou, N.J. Divins, H. Mistry, Y.-T. Chen, A. Kostka, J.A. Boscoboinik, B.R. Cuenya, Segregation phenomena in size-selected bimetallic cuni nanoparticle catalysts, J. Phys. Chem. B 122 (2018) 919–926, http://dx.doi.org/10.1021/acs.jpcb.7b06984.

[20] I. Zegkinoglou, L. Pielsticker, Z.-K. Han, N.J. Divins, D. Kordus, Y.-T. Chen, C. Escudero, V. Pérez-Dieste, B. Zhu, Y. Gao, B.R. Cuenya, Surface segregation in cuni nanoparticle catalysts during co2 hydrogenation: The role of co in the reactant mixture, J. Phys. Chem. C 123 (2019) 8421–8428, http://dx.doi.org/10.1021/acs.jpcc.8b09912.

[21] Y. An, H. Ijaz, M. Huang, J. Qu, S. Hu, The one-pot synthesis of cuni nanoparticles with a ni-rich surface for the electrocatalytic methanol oxidation reaction, Dalton Trans. 49 (2020) 1646–1651, http://dx.doi.org/10.1039/C9DT04661E.

[22] G. Guisbiers, S. Khanal, F. Ruiz-Zepeda, J. Roque de la Puente, M. José-Yacaman, Cu-ni.nano-alloy:. mixed, Core–shell or janus nano-particle? Nanoscale 6 (2014) 14630–14635, http://dx.doi.org/10.1039/C4NR05739B.

[23] M. Heilmann, C. Prinz, R. Bienert, R. Wendt, B. Kunkel, J. Radnik, A. Hoell, S. Wohlrab, A. Guilherme Buzanich, F. Emmerling, Size-tunable ni–cu core–shell nanoparticles—structure, Compos. Catal. Act. the Reverse Water–Gas Shift React. Adv. Eng. Mater. 24 (2022) 2101308, http://dx.doi.org/10.1002/adem.202101308.

[24] T. Yamauchi, Y. Tsukahara, T. Sakata, H. Mori, T. Yanagida, T. Kawai, Y. Wada, Magnetic cu–ni (core–shell) nanoparticles in a one-pot reaction under microwave irradiation, Nanoscale 2 (2010) 515–523, http://dx.doi.org/10.1039/B9NR00302A.

[25] H. Guo, J. Jin, Y. Chen, X. Liu, D. Zeng, L. Wang, D.-L. Peng, Controllable synthesis of cu–ni core–shell nanoparticles and nanowires with tunable magnetic properties, Chem. Commun. 52 (2016) 6918–6921, http://dx.doi.org/10.1039/C6CC02868C.

[26] A. Quintana, E. Menéndez, E. Isarain-Chávez, J. Fornell, P. Solsona, F. Fauth, M.D. Baró, J. Nogués, E. Pellicer, J. Sort, Tunable magnetism in nanoporous cuni alloys by reversible voltage-driven element-selective redox processes, Small 14 (2018) 1704396, http://dx.doi.org/10.1002/smll.201704396.

[27] Q. Wen, Y. Feng, H. Gu, H. Yan, Z. Yang, M. Zhu, J. Xu, Effects of reduction pretreatment on ni-cu bimetallic catalysts and their catalytic performance on co2 hydrogenation, Greenh. Gases: Sci. Technol. 15 (2025) 197–205, http://dx.doi.org/10.1002/ghg.2332.

[28] J. Shen, Z. You, S. Wang, Y. Wang, Y. Liang, S. Yuan, Low-coordinated cu-ni edge sites in bimetallic aerogels for boosting electrochemical nitrate-to-ammonia conversion, J. Hazard. Mater. 495 (2025) 139051, http://dx.doi.org/10.1016/j.jhazmat.2025.139051.

[29] N. Janvelyan, M.A. van Spronsen, C.H. Wu, Z. Qi, M.M. Montemore, J. Shan, D.N. Zakharov, F. Xu, J.A. Boscoboinik, M.B. Salmeron, E.A. Stach, M. Flyztani-Stephanopoulos, J. Biener, C.M. Friend, Stabilization of a nanoporous nicu dilute alloy catalyst for non-oxidative ethanol dehydrogenation, Catal. Sci. Technol. 10 (2020) 5207–5217, http://dx.doi.org/10.1039/D0CY00683A.

[30] K.-L. Wu, Y.-M. Cai, B.-B. Jiang, W.-C. Cheong, X.-W. Wei, W. Wang, N. Yu, Cu@ni core–shell nanoparticles/reduced graphene oxide nanocomposites for nonenzymatic glucose sensor, RSC Adv. 7 (2017) 21128–21135, http://dx.doi.org/10.1039/C7RA00910K.

[31] A. Križan, K. Zimny, A. Guyonnet, E.O. Idowu, E. Duguet, M. Plissonneau, L. d'Alençon, T. Le Mercier, M. Tréguer-Delapierre, Bimetallic copper-based nanowires and the means to create next-generation stable transparent electrodes, Nano Express 4 (2023) 042001, http://dx.doi.org/10.1088/2632-959X/ad0168.

[32] I.E. Stewart, A.R. Rathmell, L. Yan, S. Ye, P.F. Flowers, W. You, B.J. Wiley, Solution-processed copper–nickel nanowire anodes for organic solar cells, Nanoscale 6 (2014) 5980–5988, http://dx.doi.org/10.1039/C4NR01024H.

[33] B.F.Y. Rezaga, M.D.L. Balela, Synthesis and characterization of nickel-coated copper nanowires for flexible conductive thin film applications, Mater. Today: Proc. 22 (2020) 241–247, http://dx.doi.org/10.1016/j.matpr.2019.08.094.

[34] J. Xue, J. Song, Y. Zou, C. Huo, Y. Dong, L. Xu, J. Li, H. Zeng, Nickel concentration-dependent opto-electrical performances and stability of cu@cuni nanowire transparent conductors, RSC Adv. 6 (2016) 91394–91400, http://dx.doi.org/10.1039/C6RA19577F.

[35] J. Chen, J. Chen, Y. Li, W. Zhou, X. Feng, Q. Huang, J.-G. Zheng, R. Liu, Y. Ma, W. Huang, Enhanced oxidation-resistant cu–ni core–shell nanowires: controllable one-pot synthesis and solution processing to transparent flexible heaters, Nanoscale 7 (2015) 16874–16879, http://dx.doi.org/10.1039/C5NR04930J.

[36] H. Zhang, S. Wang, Y. Tian, Y. Liu, J. Wen, Y. Huang, C. Hang, Z. Zheng, C. Wang, Electrodeposition fabrication of cu@ni core shell nanowire network for highly stable transparent conductive films, Chem. Eng. J. 390 (2020) 124495, http://dx.doi.org/10.1016/j.cej.2020.124495.

[37] K. Kim, H.-C. Kwon, S. Ma, E. Lee, S.-C. Yun, G. Jang, H. Yang, J. Moon, All-solution-processed thermally and chemically stable copper–nickel core–shell nanowire-based composite window electrodes for perovskite solar cells, ACS Appl. Mater. & Interfaces 10 (2018) 30337–30347, http://dx.doi.org/10.1021/acsami.8b09266.

[38] H. Wang, C. Wu, Y. Huang, F. Sun, N. Lin, A.M. Soomro, Z. Zhong, X. Yang, X. Chen, J. Kang, D. Cai, One-pot synthesis of superfine core–shell cu@metal nanowires for highly tenacious transparent led dimmer, ACS Appl. Mater. & Interfaces 8 (2016) 28709–28717, http://dx.doi.org/10.1021/acsami.6b09009.

[39] Y. Fang, X. Zeng, Y. Chen, M. Ji, H. Zheng, W. Xu, D.-L. Peng, Cu@ni core–shell nanoparticles prepared via an injection approach with enhanced oxidation resistance for the fabrication of conductive films, Nanotechnology 31 (2020) 355601, http://dx.doi.org/10.1088/1361-6528/ab925c.

[40] A. Križan, L. Bardet, K. Zimny, M. Romanus, M. Berthe, C. Labrugère-Sarroste, D. Bellet, M. Tréguer-Delapierre, Oxidation-resistant cu-based nanowire transparent electrodes activated by an exothermic reduction reaction, ACS Nano 18 (2024) 34902–34911, http://dx.doi.org/10.1021/acsnano.4c12698.

[41] F. Baletto, C. Mottet, R. Ferrando, Molecular dynamics simulations of surface diffusion and growth on silver and gold clusters, Surf. Sci. 446 (2000) 31–45.

[42] J. Yang, W. Hu, Y. Wu, X. Dai, Diffusion and growth of nickel, iron and magnesium adatoms on the aluminum truncated octahedron: A molecular dynamics simulation, Surf. Sci. 606 (2012) 971–980, http://dx.doi.org/10.1016/j.susc.2012.02.017.

[43] J. Yang, W. Hu, Y. Wu, X. Dai, Substrate dependence of growth configurations for co–cu bimetallic clusters, Cryst. Growth & Des. 12 (2012) 2978–2985, http://dx.doi.org/10.1021/cg300195z.

[44] X. Dai, J. Yang, W. Hu, Z. Yang, S. Peng, Dynamic self-diffusion behaviors of nickel adatoms on clusters with wulff shape, Internat. J. Modern Phys. B 34 (2020) 2050015, http://dx.doi.org/10.1142/S0217979220500150.

[45] X. Dai, C. Zhu, D. Wen, W. Hu, Atomistic simulation of the surface configuration of the ni–re cluster, Thin Solid Films 737 (2021) 138938, http://dx.doi.org/10.1016/j.tsf.2021.138938.

[46] M. Gao, D. Wen, G. Cao, Y. Zhang, Y. Deng, J. Hu, Study the growth mechanism of agni nanoparticles by surface diffusion, Appl. Surf. Sci. 640 (2023) 158286, http://dx.doi.org/10.1016/j.apsusc.2023.158286.

[47] D. Nelli, C. Roncaglia, R. Ferrando, Z. Kataya, Y. Garreau, A. Coati, C. Andreazza-Vignolle, P. Andreazza, Sudden collective atomic rearrangements trigger the growth of defect-free silver icosahedra, Nanoscale 15 (2023) 18891–18900, http://dx.doi.org/10.1039/D3NR04530G.

[48] D. Nelli, F. Pietrucci, R. Ferrando, Impurity diffusion in magic-size icosahedral clusters, J. Chem. Phys. 155 (2021) 144304, http://dx.doi.org/10.1063/5.0060236.

[49] F. Cyrot-Lackmann, F. Ducastelle, Binding energies of transition-metal atoms adsorbed on a transition metal, Phys. Rev. B 4 (8) (1971) 2406.

[50] R.P. Gupta, Lattice relaxation at a metal surface, Phys. Rev. B 23 (12) (1981) 6265.

[51] V. Rosato, M. Guillope, B. Legrand, Thermodynamical and structural properties of fcc transition metals using a simple tight-binding model, Phil. Mag. A 59 (2) (1989) 321–336.

[52] G. Rossi, L. Anghinolfi, R. Ferrando, F. Nita, G. Barcaro, A. Fortunelli, Prediction of the structures of free and oxide-supported nanoparticles by means of atomistic approaches: the benchmark case of nickel clusters, Phys. Chem. Chem. Phys. 12 (2010) 8564.
[53] J.-M. Roussel, S. Labat, O. Thomas, Relation between strain and composition in coherent epitaxial cu/ni multilayers: Influence of strong concentration gradients, Phys. Rev. B 79 (2009) 014111, http://dx.doi.org/10.1103/PhysRevB.79.014111.
[54] J. Li, Basic molecular dynamics, in: Handbook of Materials Modeling: Methods, Springer, 2005, pp. 565–588.
[55] M.P. Allen, D.J. Tildesley, et al., Computer Simulation of Liquids, Clarendon, Oxford, 1987.
[56] D. Faken, H. Jónsson, Systematic analysis of local atomic structure combined with 3d computer graphics, Comput. Mater. Sci. 2 (1994) 279.
[57] C. Roncaglia, R. Ferrando, Machine learning assisted clustering of nanoparticle structures, J. Chem. Inf. Model. 63 (2023) 459–473, http://dx.doi.org/10.1021/acs.jcim.2c01203.
[58] V. Vitek, T. Egami, Atomic level stresses in solids and liquids, Phys. Status Solidi b 144 (1987) 145–156.
[59] D. Nelli, C. Roncaglia, C. Minnai, Strain engineering in alloy nanoparticles, Adv. Phys.: X 8 (2023) 2127330, http://dx.doi.org/10.1080/23746149.2022.2127330.
[60] D. Nelli, C. Roncaglia, R. Ferrando, C. Minnai, Shape changes in aupd alloy nanoparticles controlled by anisotropic surface stress relaxation, J. Phys. Chem. Lett. 12 (2021) 4609–4615, http://dx.doi.org/10.1021/acs.jpclett.1c00787.
[61] H. Lukas, S.G. Fries, B. Sundman, Computational Thermodynamics: The Calphad Method, Cambridge University Press, 2007.
[62] N. Saunders, A.P. Miodownik, CALPHAD (Calculation of Phase Diagrams): A Comprehensive Guide, vol. 1, Elsevier, 1998.
[63] F. Baletto, R. Ferrando, Structural properties of nanoclusters: Energetic, Thermodyn. Kinet. Eff. Rev. Mod. Phys. 77 (2005) 371–423.
[64] F. Montalenti, Transition-path spectra at metal surfaces, Surf. Sci. 543 (2003) 141–152, http://dx.doi.org/10.1016/j.susc.2003.08.003.
[65] H. Matter, J. Winter, W. Triftshäuser, Phase transformations and vacancy formation energies of transition metals by positron annihilation, Appl. Phys. 20 (1979) 135–140, http://dx.doi.org/10.1007/BF00885934.
[66] R.R. Bourassa, B. Lengeler, The formation and migration energies of vacancies in quenched copper, j, Ournal Phys. F: Met. Phys. 6 (1976) 1405, http://dx.doi.org/10.1088/0305-4608/6/8/003.
[67] N.Q. Lam, L. Dagens, Calculations of the properties of single and multiple defects in nickel, J. Phys. F: Met. Phys. 16 (1986) 1373, http://dx.doi.org/10.1088/0305-4608/16/10/006.
[68] L.C. Smedskjaer, M.J. Fluss, D.G. Legnini, M.K. Chason, R.W. Siegel, Positron Annihilation, North Holland Publishing, 1982.
[69] J. Wolff, M. Franz, J.-E. Kluin, D. Schmid, Vacancy formation in nickel and α-nickel-carbon alloy, Acta Mater. 45 (11) (1997) 4759–4764, http://dx.doi.org/10.1016/S1359-6454(97)00112-2.
[70] R.W. Siegel, in: J. Takamura (Ed.), Points Defects and Defect Interactions in Metals, University of Tokyo Press, Tokyo, 1982.
[71] M. Dearg, C. Roncaglia, D. Nelli, E.Y. El Koraychy, R. Ferrando, T.J.A. Slater, R.E. Palmer, Frame-by-frame observations of structure fluctuations in single mass-selected au clusters using aberration-corrected electron microscopy, Nanoscale Horiz. 9 (2024) 143–147, http://dx.doi.org/10.1039/D3NH00291H.